Draft version September 22, 2023
Typeset using LaTeX default style in AASTeX631

Rotational Components of the Sun's Mean Field

Neil R. Sheeley, Jr.[1]

[1] *Visiting Research Scientist*
Lunar and Planetary Laboratory, University of Arizona
Tucson, AZ 85721, USA

ABSTRACT

This paper uses wavelet transforms to look for the rotational frequencies of the Sun's mean line-of-sight magnetic field. For a sufficiently high wavelet frequency, the spectra of the dipole, quadrupole, and hexapole field components each show a time-dependent fine structure with periods in the range of 26.5-30 days and their harmonics. These maps confirm that a large enhancement of 30-day power occurred in the dipole field during 1989-1990, as recorded previously using Fourier techniques (Sheeley 2022). Also, during some years the maps show power at 26.5 days (or its harmonics), that is clearly distinguishable from the 26.9-27.0 day rotation period at the Sun's equator. In at least one case, the 26.5-day period was a wave phenomenon caused by the systematic eruption of active regions at progressively more western locations in the Carrington coordinate system, as if the flux were emerging from a fixed longitude in a faster rotating subsurface layer. Based on previous studies of the mean field (Sheeley et al. 1985; Sheeley & DeVore 1986; Sheeley 2022), I conclude that the enhanced wavelet patterns in this paper are regions where magnetic flux is emerging in configurations that strengthen the Sun's horizontal dipole, quadrupole, and hexapole fields, and (in the case of the more slowly rotating patterns) where this flux is being transported to mid-latitudes whose rotation periods are in the range 28-30 days.

Keywords: Solar magnetic fields (1503)— Solar rotation (1524),—Solar cycle (1487)— Stellar magnetic fields (1610)

1. INTRODUCTION

In a previous paper, I used Fourier transforms of Wilcox Solar Observatory (WSO) measurements from 16 May 1975 to 16 November 2021 to study the rotational components of the Sun's mean line-of-sight magnetic field (Sheeley 2022). With this 46.5-yr sequence of daily measurements, the transforms resolved long-lived 2-sector recurrence patterns of 27, 28.5, and 30 days, and showed the existence of 4-sector and 6-sector patterns. For suitable choices of the limits of integration, it was possible to determine the temporal origin of some of the 2-sector recurrence patterns.

Now, in this paper, I present the results of applying wavelet transforms to the WSO mean-field measurements updated though 5 July 2022. These transforms are designed to provide spectral power as a function of time and wavelet scale (equivalent to spectral frequency, ω, or period, $T = 2\pi/\omega$). The analysis differs from an earlier wavelet analysis of the WSO data by Boberg et al. (2002). They considered the general properties of oscillating structures over a broad range of periods from 90 minutes to 11 years, whereas in this study, I am focussing on the detailed spectral properties for periods comparable to the 27-day rotational period of the Sun and its second and third harmonics at 13.5 days and 9 days.

By selecting the wavelet frequency sufficiently high, I have been able to resolve the components with periods of ∼27 days from those of periods 28.5 days and 30 days. In addition, the resulting two-dimensional maps show resolved spectral power, not only for the horizontal dipole fields with azimuthal number $m = 1$ found in the earlier paper (Sheeley 2022), but also for the horizontal quadrupole ($m = 2$) and hexapole ($m = 3$) fields. As we will see, this approach verifies my previous results using Fourier transforms. Also, it reveals a long-lived quadrupole pattern in 1990-1991, having a period that is shorter than the equatorial rotation period at the Sun's surface (∼26.5 days, compared to ∼26.9-27.0 days of synodic rotation).

After describing the wavelet technique, I will show the resulting maps of spectral power (the so-called wavelet scalegrams), and present a possible interpretation of this 2-dimensional power. Appendices A and B contain derivations of mathematical relations used in the text, and Appendices C and D contain derivations of the mean field and open flux of an idealized magnetic doublet representing the flux in a nominal bipolar magnetic region.

2. ANALYSIS TECHNIQUES

2.1. *Range of Frequencies*

The WSO mean-field used in this paper consists of a single measurement every day for $N = 17,218$ days, corresponding to the 47-yr interval from 16 May 1975 to 5 July 2022. The corresponding range of frequencies can be interpreted as follows: The maximum frequency, ω_{max} (the Nyquist frequency), is determined by one point every half wave. Consequently, $\omega_{max} = \pi$ rad point^{-1}, which is π rad day^{-1} at the observing rate of 1 point day^{-1}. The minimum frequency, ω_{min}, is determined by putting $N/2$ points in the half wave, so that $\omega_{min} = \pi/(N/2) = 2\pi/N$ rad day^{-1}.

Thus, we can express the range, R, in rad day^{-1} as

$$R \;=\; \left(\frac{2\pi}{N},\; \pi\right) \;=\; \frac{2\pi}{N}\left(1,\; \frac{N}{2}\right) \;=\; \omega_{min}\left(1,\; \frac{N}{2}\right). \tag{1}$$

The smallest frequency, $\omega_{min} = 2\pi/N$, is also the spectral resolution, $\Delta\omega$, of the data. In terms of this resolution, the full set of frequencies, Ω, becomes

$$\Omega \;=\; \Delta\omega\left\{1,\; 2,\; 3,\; ...,\; (\frac{N}{2} - 1),\; \frac{N}{2}\right\}. \tag{2}$$

Of course, it was not possible to obtain mean-field measurements on every day due to a variety of conditions that presumably included adverse weather, and occasional hardware and software problems. Consequently, there were data gaps on 3069 of the 17218 days, corresponding to 17.8% of the data. On these days, I set the mean field equal to zero before computing the wavelet transforms. To get a feeling for how that may have affected the resulting maps, I also replaced those values by random numbers in the range (-0.32, +0.32) G, where 0.32 G was the root-mean-square value of the other measurements. This had essentially no effect on the distribution of wavelet power, and even when the threshold was set higher than 0.32 G, only the faint background distribution was affected. The enhanced regions of power were unchanged. I did not try interpolating between adjacent non-gap values because the gaps were not always isolated days, but came in a variety of combinations ranging from one to several days and sometimes to a few weeks or more.

2.2. *The Wavelet and the Wavelet Transform*

When using Fourier techniques, one combines the time series, f(t), with an oscillating factor, $e^{i\omega t}$, that spans the entire time series. This gives the power as a function of frequency, ω, but does not indicate when the spectral peaks of this distribution originated. With wavelets, one introduces a damping factor of the form, $e^{-(1/2)\{(t-\tau)/s\}^2}$, to limit the range of oscillation to a temporal scale, s, around the time $t = \tau$, and then combines the time series, f(t), with this damped and phase-shifted oscillation to obtain power as a function of the temporal shift, τ, and the temporal scale, s. In particular, the damped, but unshifted wavelet, ψ, analogous to the Fourier factor, $e^{i\omega t}$, is

$$\psi \sim e^{i\omega_0 t}\; e^{-\frac{1}{2}(t/s)^2} \;\sim\; e^{i\gamma(t/s)}\; e^{-\frac{1}{2}(t/s)^2}, \tag{3}$$

where γ is a dimensionless constant, indicating the number of radians of oscillation in a scale length, s. Equivalently, $\gamma/2\pi$ is the number of oscillations in a decay time scale, s. Now, ω_0 is a true frequency in rad day^{-1}, given by

$$\omega_0 \;=\; \frac{\gamma}{s}. \tag{4}$$

This differs from the conventional notation, $e^{i\omega_0(t/s)}$, in which ω_0 is regarded as a 'dimensionless frequency', and is usually taken to be a number approximately equal to 6 (Boberg et al. 2002; Podesta 2009; Torrence & Compo 1998; Shi et al. 2022). I prefer to assign another variable, γ, to the dimensionless quantity and to reserve the symbol, ω_0, for a bonafide frequency with dimensions of rad day^{-1}. For simplicity, I have omitted a normalization factor of $\pi^{-1/4}$

from these wavelet expressions, but I will include it when the actual calculations are performed. The idea is to shift this wavelet by an amount, τ, to form

$$\psi\left(\frac{t-\tau}{s}\right) \sim e^{i\gamma((t-\tau)/s)}\ e^{-\frac{1}{2}((t-\tau)/s)^2}, \tag{5}$$

and then find the value of

$$F(t,s) \ = \ \frac{1}{\sqrt{s}}\int_{-\infty}^{+\infty} B_m(\tau)\psi^*(\frac{t-\tau}{s})d\tau \ = \ \frac{\pi^{-1/4}}{\sqrt{s}}\int_{-\infty}^{+\infty} B_m(\tau)\ e^{-\frac{1}{2}\{(t-\tau)/s\}^2}e^{-i\gamma\{(t-\tau)/s\}}d\tau, \tag{6}$$

where $B_m(\tau)$ is the mean-field time series, and the factor of $\pi^{-1/4}$ has now been included in the wavelet. Also, I have interchanged the roles of t and τ so that t survives the integration and now refers to the time shift of the wavelet from its peak value. Because $F(t,s)$ is usually a complex number, we plot the real number, $F(t,s)F^*(t,s) = |F(t,s)|^2$, as a function of t (on the horizontal axis) and as a logarithmic function of spectral period, $T = 2\pi/\omega$, (on the vertical axis). In this case, the vertical axis indicates $\log_2(2T)$ increasing downward from 1 at the top of the map.

As we shall see in the next section, it will be necessary to choose $\gamma >> 6$ to resolve the individual solar rotation periods and see the effects of differential rotation. As shown in Appendix A, for such very large values of γ, there is essentially no difference between ω_0, the frequency defined by Eq(4), and ω, the frequency of the oscillating mean field, obtained from the wavelet analysis. This means that there is no need to retain the 0 on ω_0 or on $T_0 = 2\pi/\omega_0$. Finally, as a point of terminology, ψ is a Gabor wavelet that depends on γ, and for the special case of $\gamma = \pi\sqrt{2/ln2} \approx 5.336$, the Gabor wavelet reduces to what is usually called a Morlet wavelet.

3. RESULTS

Figure 1 compares the wavelet power in the WSO mean field (top panel) with the monthly averaged sunspot number from the Royal Observatory of Belgium (SILSO) shown in the lower panel. Here, $\gamma = \pi\sqrt{2/ln2} \approx 5.33$, corresponding to a Morlet wavelet transform of the WSO mean-field measurements. This is essentially what Boberg et al. (2002) obtained for the WSO data through 2001 using $\gamma = 6$. (See their Figure 1).

The oscillation period, T, is indicated in powers of 2 (like octaves of a musical scale), running logarithmically downward along the vertical axis as $\log_2(2T)$. For convenience, I use the approximation that $\log_2(2T) \approx \log_2(T/27) + 5.75$ (equivalent to $\log_2 27 \approx 4.75$), which shows directly that the 27-day equatorial rotation period occurs at 5.75 on the vertical axis. Also, I used 32 steps per octave so that

$$\log_2(2T) \ = \ 1 \ + \ \log_2 T \ = \ 1 \ + \ \frac{j}{n}, \tag{7}$$

with $n = 32$ and j running from 1 to 416 (13×32). In this case, $j = 416$ gives $\log_2(2T) = 14$. Note that $\log_2 N = \log_2 17218 \approx 14.07$, so that the ordinate values from 1 to 14 almost span the full set of 17218 measurements.

The map shows a variety of spectral and temporal features. Toward the bottom of the map where ordinate values are in the range 11-13 (corresponding to times of years), coarse structures are aligned horizontally. Near the top of the map where ordinate values are in the range 4-7 (8-64 days), fine structures are aligned vertically. In between, the transition seems to consist of a multitude of round features scattered through the ordinate range of $\log_2 2T = 7 - 9$, corresponding to periods in the range 64-256 days.

Looking more closely, we can see that the vertical fine structures are distributed in rows running horizontally at locations of 5.75 (27 days), 4.75 (27/2 days), and more faintly at 4.16 (27/3 days), corresponding to the equatorial rotation period and its second and third harmonics. These features indicate rotational contributions from the dipole, quadrupole, and hexapole moments of the Sun's field. They fall into four time intervals corresponding to sunspot cycles 21-24. Their intensities are roughly correlated with the strengths of the sunspot cycles and are relatively weak during cycle 24. However, these features are widely distributed over each sunspot cycle, and often occur early in the declining phase of the cycle, as Sheeley & Wang (2015) found in their analysis of the Sun's large-scale field.

If we represent the vertical dimension of this map by $y = \log_2(2T)$, then we can relate small changes in y to changes in the period, T. We do this by converting to natural logarithms and then differentiating to obtain

$$dy\ ln2 \ = \ \frac{dT}{T}. \tag{8}$$

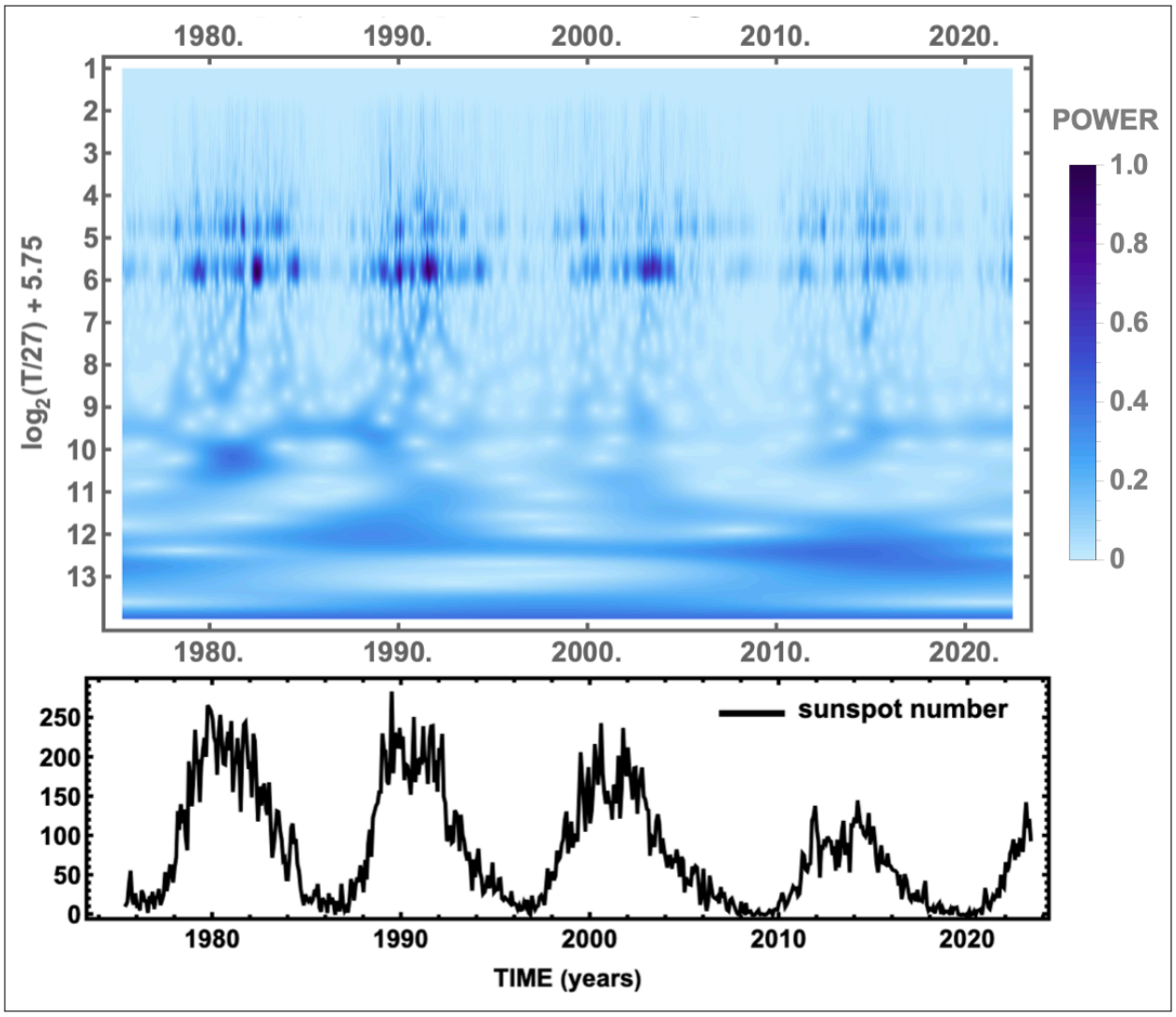

Figure 1. (top) Wavelet scaleogram of the WSO mean field measurements, showing power as a function of time, t, in years, and period, T, in days expressed logarithmically as $\log_2(T/27) + 5.75$. Here, $\gamma = \pi\sqrt{2/ln2} \approx 5.33$, corresponding to a Morlet wavelet. (bottom) Monthly averaged sunspot number from the Royal Observatory of Belgium (SILSO).

Thus, small changes of y are proportional to the fractional change $\Delta T/T$. In Figure 1, the rotational fine structures have a vertical extent of about $\Delta y = 0.5$, corresponding to $\Delta T/T = 0.5\ ln2 = 0.346$, which is $\Delta T = 9.4$ days at $T = 27$ days and 4.7 days at $T = 27/2$ days. So $\gamma = 5.33$ gives a relatively coarse picture of these rotational features. In other words, the Morlet transform shows the dipole, quadrupole and hexapole components with good temporal resolution ($\lesssim$ 1 solar rotation period), but it does not show the rotational fine structures of these components. On the other hand, with 32 pixels per octave (corresponding to $dy = 1/32$ and $dT/T = 0.02$), the display is capable of resolving features whose periods differ by $dT = 0.54$ days, which includes the 27-day, 28.5-day, and 30-day periods.

However, to achieve this spectral resolution, it is necessary to increase γ, or $\gamma/2\pi$, which is the number of waves of period, T, in a decay time, s, as indicated by Eq(4) rewritten in the form

$$s \ = \ (\frac{\gamma}{2\pi})T. \tag{9}$$

To understand this, recall from section 2.1 that a Fourier transform of the entire set of $N = 17218$ points has a frequency resolution of $1/N$ cycles day^{-1}. In other words, the frequency resolution is inversely related to the number of data points in the sample. Accordingly, we would expect wavelets of scale s to give a frequency resolution $\sim 1/s$ cycles day^{-1}. As shown in Eq(B18b) of Appendix B, the root-mean-square angular resolution is $(\Delta\omega)_{rms} = 1/(s\sqrt{2})$. Dividing by the angular frequency, ω, given by Eq(4), we obtain $\Delta\omega/\omega = 1/(\gamma\sqrt{2})$. Also, because $\Delta\omega/\omega = -\Delta T/T$,

it follows that the spectral resolution is

$$|\frac{\Delta\omega}{\omega}| \;=\; |\frac{\Delta T}{T}| \;=\; \frac{1}{\sqrt{2}}\frac{1}{\gamma}. \tag{10}$$

For a given period, $T = 27$ days, we can obtain a large value of s (corresponding to a high spectral resolution) by choosing a large value of γ. As a specific case, let's take $\gamma/2\pi = 20$, corresponding to $|\Delta T/T| = 0.0056$ and $\Delta T = 0.15$ days. Then, using Eq(9) and Eqs(B18a), we obtain

$$(\Delta t)_{rms} \;=\; \frac{s}{\sqrt{2}} \;=\; \frac{1}{\sqrt{2}}(\frac{\gamma}{2\pi})T \;=\; \frac{1}{\sqrt{2}}\times 20\times 27 \text{ days} \;=\; 381.8 \text{ days} \;=\; 1.04 \text{ yr}. \tag{11}$$

Thus, for this example of $T = 27$ days and $\gamma/2\pi = 20$, the spectral resolution is 0.15 days, which is sufficient to distinguish the 27-day, 28.5-day, and 30-day spectral features, but is obtained at the cost of degrading the temporal resolution to about 1 yr.

Figure 2 illustrates this effect by changing $\gamma/2\pi$ in powers of 2 ranging from 1 in the top panel to 16 in the bottom panel. In the top panel, the narrow slivers of power have widths on the order of a 27-day solar rotation or less. But their vertical extensions are about 0.5 unit, corresponding to several days of frequency resolution, as mentioned above. In the bottom panel where $\gamma/2\pi = 16$, the spectral features are aligned in horizontal strips of widths $\lesssim 0.03$ unit (corresponding to about 0.5 day) and separations of about 0.1 unit (corresponding to ≈ 2 days, so that the rotation periods of 27, 28.5, and 30 days are clearly resolved. These three components are especially noticeable in 1990 when the dipole field has significant power at all three frequencies.

By comparison, in the second panel from the top where $\gamma/2\pi = 2$, the distribution of wavelet power looks very much like the temporal plots of power in the $m = 1$, $m = 2$, and $m = 3$ modes, as shown in Figure 7 of Sheeley (2022). This is as one would expect because those plots were obtained by inverting the Fourier transform of the entire data set for the three frequency bands corresponding to $m = 1$, $m = 2$, and $m = 3$.

I used maps like those in Figure 2 to make a movie of the wavelet power, but with a wider and finer range of $\gamma/2\pi$. When viewed in a single-step mode, the movie allows one to investigate the transition from high temporal resolution to high spectral resolution in detail. The idea is to identify individual features and track them backward and forward as a function of $\gamma/2\pi$. In this way, one might be able to identify the separate eruptions of flux that contribute to the long-term patterns of the mean field. Figure 2 is sufficient to make these identifications for some simple cases. For example, the 30-day, 2-sector pattern in 1989-1990 seems to have originated in two bursts, one around April 1989 and the other in January 1990. Likewise, the 27-day, 2-sector pattern in 2003-2004 seems to have originated in several eruptions during that time. Although the single-step mode is not available in video streaming, the video attachment to Figure 2 has been slowed and looped in a forward-and-backward mode that may help the online reader to appreciate this approach. Further discussion of this transition between high temporal resolution and high spectral resolution is contained in Appendix B.

Figure 3 shows the wavelet power in the dipole (m=1), quadrupole (m=2), and hexapole (m=3) regions of the spectrum near 5.75, 4.75, and 4.16 on the vertical axis. In the middle and upper panels, the values of $\gamma/2\pi$ have been increased to 20 and 40 cycles per decay time, respectively, and in both panels, the display resolution has been increased to 64 pixels per octave, corresponding to $dT/T = 0.022$ and $dT = 0.27$ days. For reference, faint dotted lines are drawn at values of $T = 27$ days, 28.5 days, and 30-days in the middle panel, and at their second harmonics in the top panel. Only the line corresponding to $T = 9$ days is shown for the third harmonic in the top panel. As before, the bottom panel shows the monthly averaged sunspot number from the Royal Observatory of Belgium plotted for cycles 21-24 and the rising phase of cycle 25.

In Figure 3, the rotational fine structure is clearly visible in the dipole and quadrupole modes, and to a lesser extent in the hexapole mode. As found previously (Sheeley 2022), the splitting is mainly one-sided, ranging from the equatorial rotation period of about 27 days to 30 days, as one might expect for magnetic patterns that are subject to differential rotation at latitudes between the equator and 45° (Newton & Nunn 1951; Snodgrass 1983; Sheeley & DeVore 1986). In addition, meridional flow and the poleward component of supergranular diffusion ought to affect the rotation by making its latitudinal profile more rigid (Sheeley et al. 1987; DeVore 1987; Wang 1998). The strong 30-day period is visible for the dipole field in 1989-1990, and there is some weak 27-day power in 2022 at the start of the rising phase of sunspot cycle 25. As noted previously (Sheeley 2022), the fine structures in one sectoral mode are not reproduced in the other sectoral modes. These fine structures refer to different multipole patterns of field, and are not the same structures rotating at different rates.

figure call

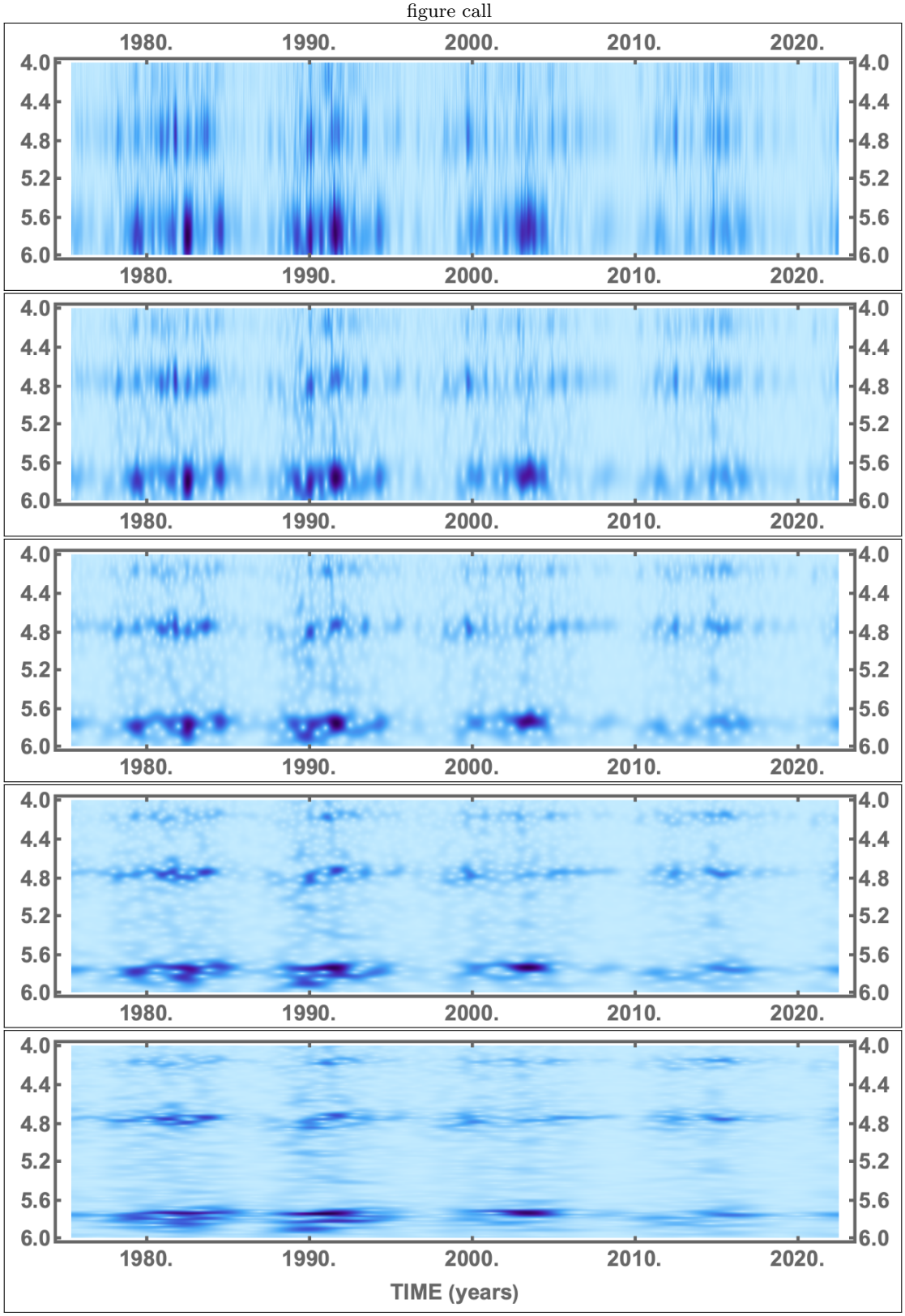

Figure 2. A sequence of Gabor scaleograms for $\gamma/2\pi = 1$ (top panel) to 16 (bottom panel) in steps of a factor of 2, showing the transition from high temporal resolution (on the horizontal axis) to high spectral resolution (on the vertical axis). The vertical axis is a logarithmic indication of spectral period, T, expressed in days as $\log_2(2T) \approx \log_2(T/27) + 5.75$. A similar sequence with a wider and finer range of $\gamma/2\pi$ is attached as a video stream. The speed of the video has been reduced and the sequence has been looped backward and forward to emphasize the transition between high temporal and spectral resolution.

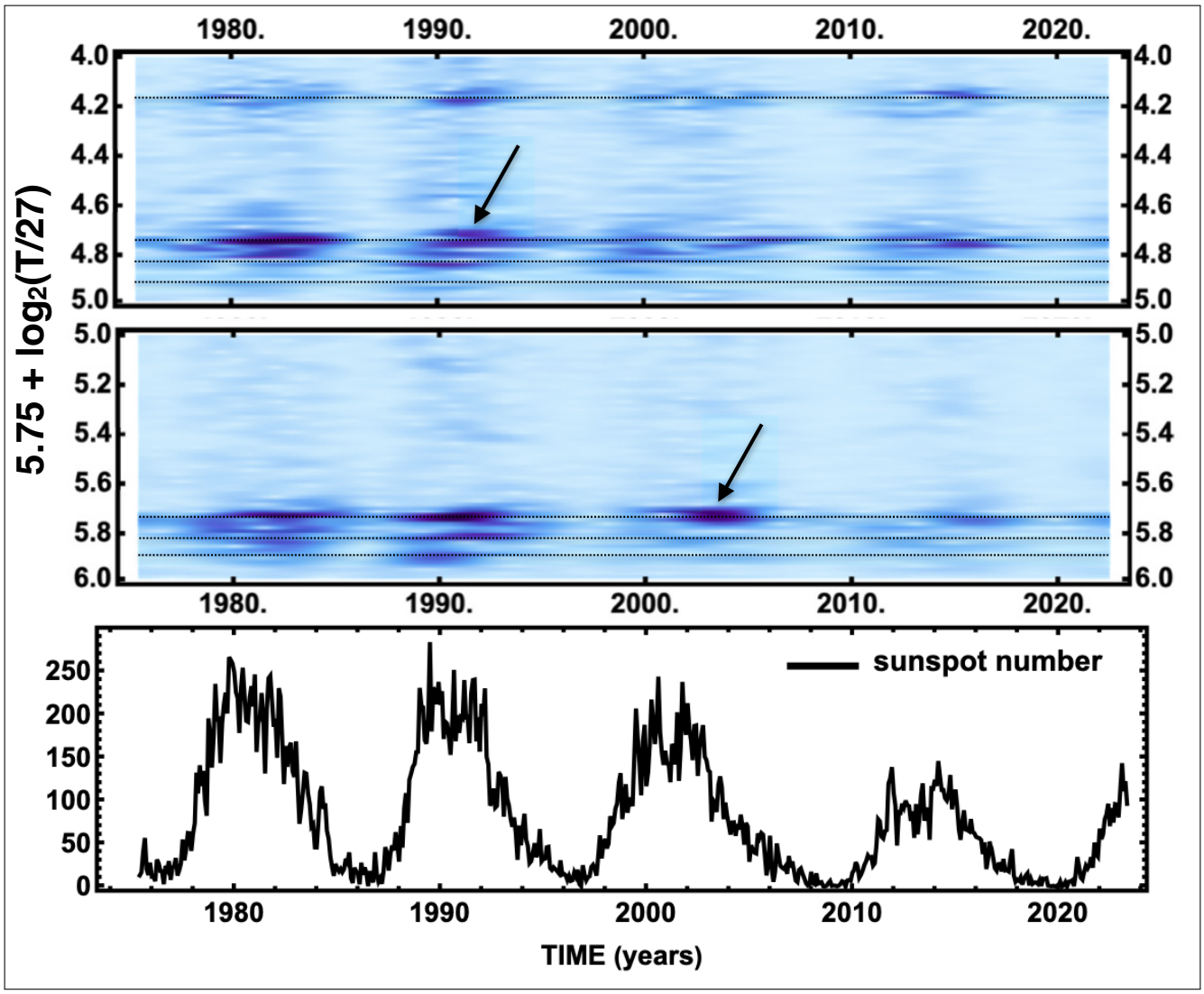

Figure 3. Wavelet power in the region of the solar rotation period (middle panel) and its second and third harmonics (top panel), displayed using $\gamma/2\pi = 20$ and $\gamma/2\pi = 40$, respectively. Faint dotted lines indicate periods of $T = 27$ days, 28.5 days, and 30 days near 5.8 on the vertical scale, and for their second harmonics near 4.8. A single dotted line indicates the third harmonic of $T = 27$ days near 4.2. The arrows indicate features at 4.73 in 1990-1991 and 5.73 during 2002-2004, corresponding to rotation periods ∼26.5 days. (bottom) Monthly averaged sunspot number from the Royal Observatory of Belgium (SILSO).

A puzzling feature of this map is the presence of power at 4.73 on the vertical scale in the years 1990-1991. This corresponds to a magnetic quadrupole rotating with a period of 13.24 days. Interpreted as a second harmonic, this would imply that the fundamental is recurring with a period of ∼26.48 days, which is noticeably smaller than the equatorial period of 26.9-27 days. There is a similar feature near 5.73 in the middle panel during 2002-2004, corresponding to a magnetic dipole field rotating with period of 26.5 days, which is again noticeably smaller than the equatorial rotation period of the Sun's surface. How can these magnetic features drift in longitude faster than the equatorial surface rotates? By means of waves, as I will explain in the next section of this paper.

4. SUMMARY AND DISCUSSION

The purpose of this paper was to see if a wavelet analysis would reveal the fine structure within each of the harmonic components of the mean field and show how that fine structure varied with time during past sunspot cycles. These objectives were achieved, but, to resolve the rotational fine structures, it was necessary to increase $\gamma/2\pi$, the number of waves per decay time of the wavelet, well beyond the value of approximately 1 that is customarily used in the

conventional Morlet transform. This was illustrated in Figures 1-3, which showed the distribution of wavelet power when $\gamma/2\pi$ ranged from 0.85 to 40.

The middle and upper panels of Figure 3 showed the rotational fine structure in the 2-sector, 4-sector, and 6-sector fields, expressed as a function of time during sunspot cycles 21-24 and early in the rising phase of cycle 25. In addition to power with the 27-day equatorial rotation period during each sunspot cycle, a substantial amount of 2-sector power was visible with a 30-day rotation period during 1989-1990, reproducing the result obtained previously using Fourier transforms (Sheeley 2022).

Figure 3 showed puzzling examples of apparent solar rotation with periods of approximately 26.5 days, noticeably lower than the 26.9-27 day equatorial rotation period of the Sun's surface. In an attempt to understand this behavior, I examined a time-lapse movie constructed from MWO Carrington maps of Ca II K-line emission during the years 1915-1979 and from NSO Carrington maps of the photospheric magnetic field during 1980-2002. This movie was made previously as part of the work for a paper on the long-term variation of K-line emission (Sheeley et al. 2011). Because these Carrington maps were displayed with the 27.27-day Carrington cadence, magnetic patterns poleward of about 15° (where the synodic rotation period is about 27.27 days) moved rapidly eastward, and features equatorward of about 15° drifted westward. The visual appearance was dramatic; high-latitude regions of each new sunspot cycle seemed to 'fly' off to the left, and the flux diffusing away from the last equatorial active regions of each cycle drifted very slowly to the right.

In addition to these obvious indications of differential rotation, there were some flux concentrations that seemed to move more rapidly to the west. Their speeds were about twice the drift speed of long-lived active regions at the Sun's equator, which is consistent with a rotation period ∼26.5 days. (A period of 26.5 days corresponds to a rotation rate of 13.58°day^{-1}, or 0.38°day^{-1} faster than the Carrington rate of 13.20°day^{-1}. By comparison, the 26.9-day equatorial rate is 13.38°day^{-1}, or 0.18°day^{-1} faster than the Carrington rate. Thus, in the Carrington maps, the 26.5-day feature moves westward at a rate that is 0.38/0.18 = 2.1 times faster than flux drifting at the equatorial rate.)

However, a close examination of the movie showed that these fast westward motions were not due to the differential rotation of long-lived magnetic regions. Rather, they were waves - apparent motions caused by the emergence of new active regions at progressively more western longitudes in the Carrington frame. Similar wavelike motions have been observed previously in Carrington stackplots of the NSO magnetic measurements by Gaizauskas et al. (1983). In fact, their oxymoron, 'simple complex IIIa', is a very clear example of this fast wavelike motion in the N10-40° latitude band during Carrington rotations 1656-1659 (14 June - 03 September 1977). My measurements of their Figure 2 give an effective rotation period of 26.3 days, compared to their value of 26.5 days. But the essential point is that the period was significantly smaller than the 26.9-27.0-day equatorial rotation period of the Sun. Consequently, the motion cannot be caused by longitudinal transport of flux by solar rotation, at least at the Sun's surface.

It is interesting that the 26.5-day period obtained from our wavelet measurements is nearly the same as the ∼26.4-day equatorial rotation period found at a depth of $0.06R_\odot$ (∼42 Mm) using GONG helioseismology measurements (Howe 2009). Thus, the fast wavelike motion in Figure 3 occurs as if the flux were emerging from a fixed longitude at that depth. In terms of the popular word, 'nesting' which Castenmiller et al. (1986) introduced for repeated eruptions of sunspot activity at the same location (see also the reviews by van Driel-Gesztelyi & Green (2015) and by Hathaway (2015)), we could call this fast wavelike motion 'subsurface nesting'.

This raises the question of whether all of the enhanced wavelet patterns of the mean field are due to nesting. We know that the long-lived recurrent patterns of 28-30-day periods owe their existence to the continued emergence of bipolar regions with their polarities in phase. Otherwise, differential rotation winds up their flux and leaves a weaker field rotating with the 27-day period of the unwound flux at the equator. This is consistent with our more recent demonstration that the mean field is dominated by the horizontal dipole and quadrupole fields (and to a lesser extent the hexapole field) (Sheeley 2022). So, the active regions must emerge in a way that reinforces the lower-order multipoles of the non-axisymmetric field. It does not matter whether this systematic emergence occurs in active longitudes as described by Gaizauskas et al. (1983), or whether it occurs by chance as in the randomized doublets of Sheeley & DeVore (1986). More recently, Hudson et al. (2014) have discussed this effect as a way of reinforcing long-lived polarity patterns at Hale sector boundaries.

It is interesting that when Sheeley & DeVore (1986) removed supergranular diffusion and meridional flow from their simulations during the declining phase of the sunspot cycle (when all of the sources emerged below 20° latitude), the 28-29-day recurrence patterns disappeared. In other words, a poleward component of transport was essential for

obtaining the 28-29-day periods, and with this transport, the slowly rotating patterns could be obtained from the flux in low-latitude active regions (providing that they continued to emerge in phase.

Also, this is consistent with the results of Sheeley et al. (1987), who found that the large-scale field rotates differentially when the source rate is high, but begins to weaken and rotate rigidly with the 27-day equatorial period when the flux stops emerging and the surviving non-equatorial flux migrates poleward and is eliminated by differential rotation and supergranular diffusion. Thus, it seems likely that spectrally resolved wavelet patterns correspond to active-region nests at different latitudes and with strong horizontal dipole and/or quadrupole moments. Wavelet maps like those in Figure 3 indicate the sunspot-cycle distribution of those nests, and γ-sequences, like those in Figure 2, provide a way of finding the individual sources that maintain the strengths of these patterns.

I am grateful to Kristopher Klein (LPL/UA) for suggesting wavelet transforms as a way of tracking solar features of different rotational periods. Also, I am grateful to Chen Shi (UCLA) for providing details of how he made wavelet maps of the radial component of the interplanetary magnetic field observed at the Parker Solar Probe. Wilcox Solar Observatory data used in this study were obtained *via* the web site http://wso.stanford.edu courtesy of J.T. Hoeksema. NSO data were acquired by SOLIS instruments operated by NISP/NSO/AURA/NSF. Sunspot numbers were obtained from WDC-SILSO, Royal Observatory of Belgium, Brussels.

APPENDIX

A. RELATIONS BETWEEN ω AND ω_0

As described in Sections 2.1 and 2.2 of the text, the basic concepts of wavelets and wavelet transforms are relatively straightforward. The most difficultly I had was in describing the quantity that was plotted on the vertical axis of the map of wavelet power. In principle, it ought to be the logarithm of the wavelet scale, $\log_2 s$. But in practice, what I really wanted was a logarithmic measure of of the oscillation frequency, ω, or equivalently, its corresponding period, $T = 2\pi/\omega$. Consequently, I needed to find a suitable relation between wavelet scale and period similar to what others have obtained in the past using a different notation for the wavelet frequency and a more limited range of $\gamma/2\pi$ (Boberg et al. 2002; Podesta 2009; Torrence & Compo 1998; Shi et al. 2022; Wolfram Research, Inc. 2023). I proceeded as follows:

First, I note that the Gaussian decay factor, $e^{-(1/2)(t/s)^2}$, does not change the frequency of the wavelet because its Fourier transform, $\hat{\psi}(\omega)$ varies as $e^{-(1/2)(\gamma-\omega s)^2}$, which peaks at $\omega = \gamma/s = \omega_0$. However, to be admissible as a wavelet, ψ must have a mean value of zero (Farge 1992; Torrence & Compo 1998), which can be achieved by subtracting a constant term from the oscillating factor, and then adjusting that term so that $\int_{-\infty}^{\infty} \psi(t,s)dt = 0$. In this case, the constant term is $e^{-\gamma^2/2}$, and the shifted wavelet becomes

$$\psi\left(\frac{t-\tau}{s}\right) \sim e^{-\frac{1}{2}((t-\tau)/s)^2} \left[e^{i\gamma((t-\tau)/s)} - e^{-\gamma^2/2}\right]. \tag{A1}$$

Now, the Fourier transform changes to

$$\hat{\psi}(\omega) = sA\sqrt{2\pi}\left[e^{-\frac{1}{2}(\gamma-\omega s)^2} - e^{-\gamma^2/2}\, e^{-\frac{1}{2}(\omega s)^2}\right], \tag{A2}$$

where $A = \pi^{-1/4}s^{-1/2}[1 + e^{-\gamma^2} - 2e^{-(3/4)\gamma^2}]^{-1/2}$ is a normalization constant chosen so that $\int_{-\infty}^{\infty} \psi\psi^* dt = 1$. With this change, the location of the peak of $\hat{\psi}(\omega)$ changes, and it is necessary to find its new location by computing $\partial\hat{\psi}/\partial\omega$ and setting it equal to 0. This gives the relation

$$e^{\gamma^2 x} = \frac{x}{x-1} \tag{A3}$$

where $x = \omega/\omega_0$. For the exponential to become large, the value of x on the right hand side of this equation must approach 1. Consequently, we can set $x = 1+\epsilon$ and solve for the small quantity, ϵ. The result is $\epsilon \approx e^{-\gamma^2}$. Therefore,

$$x = \frac{\omega}{\omega_0} \approx 1 + e^{-\gamma^2}, \tag{A4}$$

and the correction is less than 1% for $\gamma \geq 2.14$. We can find a second-order correction, δ, by defining $x_1 = 1+e^{-\gamma^2}$, and substituting $x = x_1 - \delta$ into Eq(A3). After some algebra, we obtain $\delta = x_1 - \{1 - e^{-\gamma^2 x_1}\}^{-1}$, and $x = \{1 - e^{-\gamma^2 x_1}\}^{-1}$.

This second-order solution lies within 2% of the numerical solution of Eq(A3) for $\gamma = 1$, and rapidly agrees to better than 1% as δ exceeds 1.25.

So the frequency of the wavelet is very close to ω_0. What about the frequency obtained from the wavelet transform? To find out, I will compute the wavelet power $|F(t,s)|^2$ for a time series of angular frequency, ω, given by $\cos\omega t$, and look for the value of s that makes this power a maximum. This will provide another relation between ω and s, that can be combined with Eq(4) to relate ω and ω_0. For this purpose, we return to Eq(6) where we set $B_m(t) = \cos\omega t$ and use the value of ψ given by Eq(A1):

$$F(t,s) \;=\; \frac{1}{\sqrt{s}}\int_{-\infty}^{+\infty} \cos\omega t\ \psi^*(\frac{t-\tau}{s})d\tau \;=\; \frac{\pi^{-1/4}}{\sqrt{s}}\int_{-\infty}^{+\infty} \cos\omega t\ e^{-\frac{1}{2}\{(t-\tau)/s\}^2}[e^{-i\gamma\{(t-\tau)/s\}} \;-\; e^{-\gamma^2/2}]d\tau. \tag{A5}$$

Evaluating this integral, we obtain

$$F(t,s) \sim s^{1/2}e^{-\gamma^2/2}\left[\cos\omega t\{\cosh(\gamma\omega s) - 1\} \;-\; i\ \sin\omega t\sinh(\gamma\omega s)\right], \tag{A6}$$

where constant factors depending on π have been dropped. Next, because $F(t,s)$ is a complex number, we multiply $F(t,s)$ by its complex conjugate to obtain

$$|F(t,s)|^2 \sim se^{-\gamma^2}\ [\cosh(\gamma\omega s) - 1]\ [\cosh(\gamma\omega s) - \cos 2\omega t]. \tag{A7}$$

At this point, we recognize that $\omega s \gtrsim \gamma$, in which case $\cosh(\gamma\omega s) \gtrsim \cosh(\gamma^2) >> 1$. Consequently, Eq(A7) reduces to

$$|F(t,s)|^2 \sim se^{-\gamma^2}\cosh^2(\gamma\omega s), \tag{A8}$$

and $|F(t,s)|$ becomes

$$|F(t,s)| \sim s^{1/2}e^{-\gamma^2/2}\cosh(\gamma\omega s). \tag{A9}$$

It is interesting to note that if we had ignored the $e^{-\gamma^2/2}$ term in Eq(A1) from the beginning, we would have obtained

$$|F(t,s)|^2 \sim se^{-\gamma^2}e^{-(\omega s)^2}\ [\cosh^2(\gamma\omega s) - \cos^2\omega t] \tag{A10}$$

instead of Eq(A7). Then, the condition that $\cosh^2(\gamma\omega s) >> \cos^2\omega t$ would have led to Eq(A8) and Eq(A9). This means that the approximation that we used to get there the first time is equivalent to neglecting the extra term in the wavelet that arose when we forced $\int_{-\infty}^{\infty}\psi dt = 0$. So, looking ahead, whatever we find from Eq(A9) will be produced by the original wavelet without the extra $e^{-\gamma^2/2}$ term.

Now, let us use Eq(A9) to evaluate $\partial|F(t,s)|/\partial s$ and then set it equal to 0 to find the value of s that makes $|F(t,s)|$ a maximum. The derivative is

$$\frac{\partial|F(t,s)|}{\partial s} \;=\; \frac{e^{-(\omega s)^2/2}}{2\sqrt{s}}\left[-\{2(\omega s)^2 - 1\}\cosh(\gamma\omega s) + 2(\gamma\omega s)\sinh(\gamma\omega s)\right], \tag{A11}$$

and the resulting equation for s is

$$\tanh(\gamma\omega s) \;=\; \frac{2(\omega s)^2 - 1}{2(\gamma\omega s)}. \tag{A12}$$

Substituting $s = \gamma/\omega_0$ from Eq(4), and converting from the hyperbolic tangent to ordinary exponentials, we obtain

$$e^{2\gamma^2 x} \;=\; \frac{x + x^2 - \frac{1}{2\gamma^2}}{x - x^2 + \frac{1}{2\gamma^2}}, \tag{A13}$$

where $x = \omega/\omega_0$. Eq(A13) is analogous to Eq(A3), and can be solved the same way. As before, we assume that the denominator of the right hand side is close to 0, and solve for the positive root of $x - x^2 + (1/2\gamma^2) = 0$. The result is

$$x \;=\; \frac{\omega}{\omega_0} \;=\; (1/2)\left[1 + \sqrt{1 + \frac{2}{\gamma^2}}\right], \tag{A14}$$

consistent with Eq(B8) of Podesta (2009) using slightly different notation.

If we regard Eq(A14) as the first-order solution, x_1, then we can write $x = x_1 - \epsilon$ and substitute it into Eq(A13) to obtain $\epsilon = [2x_1/(2x_1 - 1)]\ e^{-2\gamma^2 x_1}$ as the second-order correction. In this case, the second-order solution for x becomes

$$x \ = \ \frac{\omega}{\omega_0} \ = \ x_1 - \left(\frac{2x_1}{2x_1 - 1} \right) e^{-2\gamma^2 x_1}, \tag{A15}$$

where x_1 is the first-order solution given by Eq(A14). Thus, for $\gamma \gtrsim 6$, this second-order correction is negligible and the first-order solution, given by Eq(A14), is accurate to about 1%. There is no difference between ω and ω_0 for the larger values of γ that resolve the 27-day, 28.5-day, and 30-day components of differential rotation. For smaller values of $\gamma/2\pi$, one can use Eqs(A14) and (A15).

B. THE TRANSITION BETWEEN HIGH SPECTRAL AND SPATIAL RESOLUTION

Regardless of the values of s and ω_0 (or γ), the wavelet and its Fourier transform satisfy the Heisenberg uncertainty principle in the form $\Delta\omega\Delta t = 1/2$, provided that $\Delta\omega$ and Δt are both defined as the root-mean-square differences from their average values. As mentioned below, this provides a basis for understanding the transition between the maps of high spectral resolution and high spatial resolution like those shown in Figure 2.

Let's begin with $\psi(t)$ and its Fourier transform, $\hat{\psi}(\omega)$:

$$\psi(t) \ = \ e^{-\frac{1}{2}(t/s)^2} e^{i\omega_0 t}, \tag{B16a}$$

$$\hat{\psi}(\omega) \ = \ \int_{-\infty}^{\infty} \psi(t) e^{-i\omega t} dt \ = \ \sqrt{2} s \sqrt{\pi} e^{-(s^2/2)(\omega - \omega_0)^2}. \tag{B16b}$$

In this case, the mean squared averages are

$$< (\Delta t)^2 > \ = \ \frac{\int_{-\infty}^{\infty} t^2 \psi(t) \psi^*(t) dt}{\int_{-\infty}^{\infty} \psi(t) \psi^*(t) dt} \ = \ \frac{s^2}{2}, \tag{B17a}$$

$$< (\Delta\omega)^2 > \ = \ \frac{\int_{-\infty}^{\infty} (\omega - \omega_0)^2 \hat{\psi}(\omega) \hat{\psi}^*(\omega) d\omega}{\int_{-\infty}^{\infty} \hat{\psi}(\omega) \hat{\psi}^*(\omega) d\omega} \ = \ \frac{1}{2s^2}. \tag{B17b}$$

Consequently, the root-mean-square values are

$$(\Delta t)_{rms} \ = \ \frac{s}{\sqrt{2}}, \tag{B18a}$$

$$(\Delta\omega)_{rms} \ = \ \frac{1}{s\sqrt{2}}, \tag{B18b}$$

and their product is

$$(\Delta\omega)_{rms} (\Delta t)_{rms} \ = \ \frac{1}{2}, \tag{B19}$$

independent of s. Also, if the energy, E, of the wave packet were $E = \hbar\omega$, then

$$(\Delta E)_{rms} (\Delta t)_{rms} \ = \ \frac{\hbar}{2}, \tag{B20}$$

which is the conventional form of the Heisenberg uncertainty principle.

As mentioned in the text, the spectral resolution varies as $1/s$, so that Eq(B18b) gives the spectral resolution in terms of the scale, s. Likewise, Eq(B18a) gives the temporal resolution in terms of s. When combined with Eq(9) of Section 3 ($s = (\gamma/2\pi)T$), these equations provide a way of calculating these resolutions as a function of $\gamma/2\pi$, and therefore of tracking the evolution of wavelet power from high temporal resolution to high spectral resolution as was done in Figure 2.

Let's pursue this matter further by recalling from Figure 2 that well-defined frequencies in the high spectral resolution maps (with $\gamma/2\pi \sim 8 - 16$) typically correspond to bursts of short-lived features in the high temporal resolution maps (with $\gamma/2\pi \sim 1$). In particular, the quadrupole feature at 4.73 on the vertical axis during 1990-1991 (also marked by an arrow in Figure 3) corresponds to a 0.5-yr burst of 2-3 short-lived features in the high temporal resolution maps at the top of Figure 2. Other bursts are visible with lifetimes ranging from 0.4 yr to about 1 yr. The closely spaced

doublet at 4.73-4.75 during 2002-2004 (also marked by an arrow in Figure 3) corresponds to one of the strongest and longest-lived bursts in the high spatial resolution maps. And, as mentioned in Section 3, the 30-day 2-sector pattern in 1989-1990 seems to have originated in separate bursts in April 1989 and January 1990.

It is tempting to wonder if some of these temporal components are produced by the interference between closely spaced frequencies in the high spectral resolution maps, analogous to the periodic stripes that occur in Bartels displays of interplanetary magnetic field polarity when long-lived patterns of 27 days and 28.5 days overlap in time (Svalgaard & Wilcox 1975; Wang & Sheeley 1994). However, the resulting 'beat' frequencies correspond to periods that are somewhat larger than the durations of these bursts. In fact, 27-day and 28.5-day features give a period of $27\times28.5/1.5 = 513$ days = 1.4 yr, and the other frequency pairs give even larger periods. This does not include the damping associated with the wavelet scale, s, and additional work is necessary to resolve this issue with confidence. Meanwhile, I suppose that these components of temporal fine structure are enhancements of the Sun's equatorial dipole, quadrupole, and hexapole moments caused by the ongoing emergence of active regions in 'nests' rotating with 27-day, 28.5-day, and other periods.

C. THE MEAN-FIELD OF A PHOTOSPHERIC DOUBLET

Having arrived at the idea that the mean field is due to the suitable juxtaposition of magnetic doublets, I am interested to know what the contribution of a single doublet is, and the circumstances under which it could appreciably affect the mean field. An idealized magnetic doublet can be represented by an expression of the form

$$B_r \;=\; \frac{\Phi_0}{R^2}\left[\frac{\delta(\phi-\phi_L)\delta(\theta-\theta_L)}{\sin\theta_L} \;-\; \frac{\delta(\phi-\phi_F)\delta(\theta-\theta_F)}{\sin\theta_F}\right], \tag{C21}$$

where L and F refer to the leader and follower poles of the doublet, respectively, and the delta functions indicate the concentrated nature of those poles. It is easy to confirm that this magnetic doublet satisfies

$$\int_0^{\pi}\int_0^{2\pi} B_r(\theta,\phi)R^2\sin\theta d\theta d\phi \;=\; \Phi_0-\Phi_0 \;=\; 0. \tag{C22}$$

To obtain the mean field of this doublet, we simply evaluate the integral

$$B_m \;=\; \frac{1}{\pi}\int_0^{\pi}\int_0^{\pi} B_r(\theta,\phi)(\sin\theta\cos\phi)^2\sin\theta d\theta d\phi. \tag{C23}$$

The result is

$$B_m \;=\; (\frac{\Phi_0}{\pi R^2})\left[\sin^2\theta_L\cos^2\phi_L \;-\; \sin^2\theta_F\cos^2\phi_F\right]. \tag{C24}$$

Next, we define the separations between the leader and follower poles and their mid-points by $\theta_L = \theta_0 + \Delta\theta/2$, $\theta_F = \theta_0 - \Delta\theta/2$, $\phi_L = \phi_0 + \Delta\phi/2$, and $\phi_F = \phi_0 - \Delta\phi/2$, where $\Delta\theta$ and $\Delta\phi$ are the pole separations and θ_0 and ϕ_0 are the mid-points between the respective poles. Substituting these relations into Eq(C23) and using the small-angle relations for $\Delta\theta$ and $\Delta\phi$, we obtain

$$B_m \approx (\frac{\Phi_0\Delta\theta}{\pi R^2})\cos^2\phi_0\sin 2\theta_0 \;-\; (\frac{\Phi_0\Delta\phi}{\pi R^2})\sin^2\theta_0\sin 2\phi_0. \tag{C25}$$

Now, let's evaluate the root-mean-square value of the expression in Eq(C24) using the relation $< B_m^2 > \;=\; \int_0^{\pi} B_m^2 d\phi_0 / \int_0^{\pi} d\phi_0$. The result is

$$< B_m^2 > \;=\; \frac{3}{8}(\frac{\Phi_0\Delta\theta}{\pi R^2})^2\sin^2 2\theta_0 \;+\; \frac{1}{2}(\frac{\Phi_0\Delta\phi}{\pi R^2})^2\sin^4\theta_0. \tag{C26}$$

If we neglect $\Delta\theta$ compared to $\Delta\phi$ and take the square root, we obtain

$$B_m^{rms} \;=\; \frac{1}{\sqrt{2}}(\frac{\Phi_0\Delta\phi}{\pi R^2})\sin^2\theta_0. \tag{C27}$$

Thus, the rms mean field of a doublet, located near the equator where $\theta_0 = \pi/2$, is roughly equal to its doublet moment, $\Phi_0\Delta\phi$, divided by the area of the visible disk, πR^2. More accurately, $B_m^{rms} \approx 0.707(\Phi_0\Delta\phi/\pi R^2)$.

If this idealized magnetic doublet has a pole strength $\Phi_0 = 10{\times}10^{21}$Mx and a longitudinal pole separation $\Delta\phi \sim 10^\circ$ ($\sim 10^5$ km), corresponding to a mid-sized active region, then its contribution to the Sun's mean field would be only about 0.08 G. This is an order of magnitude smaller than the 1 G peaks that typically occur when the Sun's equatorial dipole and quadrupole moments are strong. To achieve these strong fields, it would take a nest of several large bipolar magnetic regions arranged with their polarities in phase, as we have found in spatially resolved observations around sunspot maximum and during the initial declining phase of the sunspot cycle (Sheeley & Wang 2015).

D. THE OPEN FLUX OF A PHOTOSPHERIC DOUBLET

Here, we extend the previous calculation to determine how much open flux is contributed by the idealized magnetic doublet given by Eq(C20). To obtain this open flux, we assume a potential field whose angular components, B_θ and B_ϕ vanish at a spherical source surface located at a radial distance R_{ss}, and whose radial component, B_r matches the radial component of the doublet field given by Eq(C20) . Eventually, we will select $R_{ss} = 2.5R$, where R is the solar radius, but, for the moment, let's consider a general value of R_{ss}. Our objective is to find the source surface field and then integrate its positive value over the source surface.

Rather than repeating the solution of this well-known boundary-value problem, I will take the solution from Eq(4a) of a previous paper by Nash et al. (1988). Setting $r = R_{ss}$ in their equation, the source-surface field becomes:

$$B_{ss} \;=\; B_r(R_{ss},\theta,\phi) \;=\; \sum_{l=0}^{\infty}\sum_{m=-l}^{l}\left[\frac{(2l+1)(R/R_{ss})^{l+2}}{l+1+l(R/R_{ss})^{2l+1}}\right] c_{lm}Y_l^m(\theta,\phi), \tag{D28}$$

where c_{lm} are the spherical harmonic components of the doublet, given by

$$B_{ph} \;=\; \sum_{l=0}^{\infty}\sum_{m=-l}^{l} c_{lm}Y_l^m(\theta,\phi). \tag{D29}$$

When B_{ph} is given by the doublet field of Eq(C20) with $\theta_L = \theta_F = \theta$ and $\phi_L - \phi_F = \Delta\phi << \pi/2$, the solution to Eq(D28) is

$$c_{lm} \;=\; -\,imN_{lm}P_l^m(0)\left(\frac{\Phi_0\Delta\phi}{R^2}\right), \tag{D30}$$

where $i = \sqrt{-1}$, $N_{lm} = \sqrt{\frac{2l+1}{4\pi}\frac{(l-m)!}{(l+m)!}}$, and $P_l^m(0)$ is an Associated Legendre polynomial function of x evaluated at $x = 0$.

Next, we suppose that the resulting field will be dominated by the contributions of the horizontal dipole and quadrupole, and limit the sum in Eq(D27) to terms of the form $Y_1^{\pm1}$ and $Y_2^{\pm2}$. In this case, the source-surface field is

$$B_{ss}(\theta,\phi) \;=\; a\sin\theta\sin\phi \;+\; b\sin^2\theta\sin 2\phi, \tag{D31}$$

where

$$a \;=\; \frac{3}{4}\left[\frac{3(R/R_{ss})^3}{2+(R/R_{ss})^3}\right]\left(\frac{\Phi_0\Delta\phi}{\pi R^2}\right) \;\approx\; \frac{9}{8}(\frac{R}{R_{ss}})^3\left(\frac{\Phi_0\Delta\phi}{\pi R^2}\right) \tag{D32}$$

and

$$b \;=\; \frac{15}{8}\left[\frac{5(R/R_{ss})^4}{3+2(R/R_{ss})^5}\right]\left(\frac{\Phi_0\Delta\phi}{\pi R^2}\right) \;\approx\; \frac{25}{8}(\frac{R}{R_{ss}})^4\left(\frac{\Phi_0\Delta\phi}{\pi R^2}\right). \tag{D33}$$

It is interesting that $b/a \approx (25/9)(R/R_{ss})$, which is approximately 1.11 when R_{ss}/R has the conventional value of 2.5. Thus, $a \sim b$, so that the horizontal dipole and quadrupole probably make comparable contributions to the open flux. In fact, we can confirm this by evaluating their separate integrals over the regions of positive flux:

$$\Phi_{open} \approx \frac{9}{8\pi}(\frac{R}{R_{ss}})\int_0^\pi \sin^2\theta\sin\theta d\theta\int_0^\pi \sin\phi d\phi\;(\Phi_0\Delta\phi) \;=\; \frac{9}{8}(\frac{R}{R_{ss}})(\Phi_0\Delta\phi) \;=\; 0.45\;(\Phi_0\Delta\phi) \tag{D34}$$

for the dipole field, and

$$\Phi_{open} \approx (\frac{25}{8\pi})(\frac{R}{R_{ss}})^2\int_0^\pi \sin^2\theta d\theta\;\;2\int_0^{\pi/2}\sin 2\phi d\phi\;(\Phi_0\Delta\phi) \;=\; (\frac{25}{3\pi})(\frac{R}{R_{ss}})^2\;(\Phi_0\Delta\phi) \;=\; 0.42\;(\Phi_0\Delta\phi) \tag{D35}$$

for the quadrupole field. The extra factor of 2 in Eq(D34) allows for the fact that the quadrupole has 2 separate quadrants of positive field. The result that $\Phi_{open} = 0.45(\Phi_0\Delta\phi)$ in Eq(D33) agrees with Eq(1) of Sheeley & Wang (2015), and its derivation in Eqs(D27)-(D33) provides the documentation for the steps that were only outlined there.

When both harmonics are present at the same time, we can obtain the positive flux by numerically integrating the absolute value of the field over the entire sphere and dividing the result by 2. Schematically, the flux is given by

$$\Phi_{open} \;=\; \frac{1}{2}\int_0^{\pi}\int_0^{2\pi} |p\sin\theta\sin\phi + q\sin^2\theta\sin 2\phi|\sin\theta d\theta d\phi \;(\Phi_0\Delta\phi), \tag{D36}$$

where $p = aR_{ss}^2/(\Phi_0\Delta\phi) \approx (9/8\pi)(R/R_{ss}) = 0.143$ and $q = bR_{ss}^2/(\Phi_0\Delta\phi) \approx (25/8\pi)(R/R_{ss})^2 = 0.159$. The result is

$$\Phi_{open} \;=\; 0.55\;(\Phi_0\Delta\phi). \tag{D37}$$

So when both the horizontal dipole and quadrupole are included, the amount of open flux is approximately $0.55(\Phi_0\Delta\phi)$ where the approximation was obtained by neglecting terms of order $(R/R_{ss})^3 = (0.4)^3 = 0.064$ in the expression for a and $(0.4)^5 = 0.010$ in b. Without this approximation, the combined open flux drops slightly to 0.54 of the doublet moment, mainly due to a drop of the dipole contribution from 0.45 to 0.44. The essential point is that for a current-free corona, the open flux of an idealized doublet located near the equator is about half of its doublet moment. This is comparable to $0.71(\Phi_0\Delta\phi)$, the flux obtained from Eq(C26) by multiplying the rms mean field by the area of the visible solar disk. Like the mean field, several suitably arranged doublets of modest size will be required to contribute appreciably to the amount of open flux.

REFERENCES

Boberg, F., Lundstedt, H., Hoeksema, J. T., Scherrer, P. H., & Liu, W. 2002, Journal of Geophysical Research: Space Physics, 107, SSH 15, doi: https://doi.org/10.1029/2001JA009195

Castenmiller, M. J. M., Zwaan, C., & van der Zalm, E. B. J. 1986, SoPh, 105, 237, doi: 10.1007/BF00172045

DeVore, C. R. 1987, SoPh, 112, 17, doi: 10.1007/BF00148484

Farge, M. 1992, Annual Review of Fluid Mechanics, 24, 395, doi: 10.1146/annurev.fl.24.010192.002143

Gaizauskas, V., Harvey, K. L., Harvey, J. W., & Zwaan, C. 1983, ApJ, 265, 1056, doi: 10.1086/160747

Hathaway, D. H. 2015, Living Reviews in Solar Physics, 12, 4, doi: 10.1007/lrsp-2015-4

Howe, R. 2009, Living Reviews in Solar Physics, 6, 1, doi: 10.12942/lrsp-2009-1

Hudson, H. S., Svalgaard, L., & Hannah, I. G. 2014, SSRv, 186, 17, doi: 10.1007/s11214-014-0121-z

Nash, A. G., Sheeley, N. R., J., & Wang, Y. M. 1988, SoPh, 117, 359, doi: 10.1007/BF00147253

Newton, H. W., & Nunn, M. L. 1951, MNRAS, 111, 413, doi: 10.1093/mnras/111.4.413

Podesta, J. J. 2009, ApJ, 698, 986, doi: 10.1088/0004-637X/698/2/986

Sheeley, N. R., J., Cooper, T. J., & Anderson, J. R. L. 2011, ApJ, 730, 51, doi: 10.1088/0004-637X/730/1/51

Sheeley, N. R., J., & DeVore, C. R. 1986, SoPh, 104, 425, doi: 10.1007/BF00159092

Sheeley, N. R., J., DeVore, C. R., & Boris, J. P. 1985, SoPh, 98, 219, doi: 10.1007/BF00152457

Sheeley, N. R., J., Nash, A. G., & Wang, Y. M. 1987, ApJ, 319, 481, doi: 10.1086/165472

Sheeley, N. R., J., & Wang, Y. M. 2015, ApJ, 809, 113, doi: 10.1088/0004-637X/809/2/113

Sheeley, N. R. 2022, The Astrophysical Journal, 937, 87, doi: 10.3847/1538-4357/ac86d6

Shi, C., Panasenco, O., Velli, M., et al. 2022, ApJ, 934, 152, doi: 10.3847/1538-4357/ac7c11

Snodgrass, H. B. 1983, ApJ, 270, 288, doi: 10.1086/161121

Svalgaard, L., & Wilcox, J. M. 1975, SoPh, 41, 461, doi: 10.1007/BF00154083

Torrence, C., & Compo, G. P. 1998, Bulletin of the American Meteorological Society, 79, 61, doi: 10.1175/1520-0477(1998)079⟨0061:APGTWA⟩2.0.CO;2

van Driel-Gesztelyi, L., & Green, L. M. 2015, Living Reviews in Solar Physics, 12, 1, doi: 10.1007/lrsp-2015-1

Wang, Y. M. 1998, in Astronomical Society of the Pacific Conference Series, Vol. 154, Cool Stars, Stellar Systems, and the Sun, ed. R. A. Donahue & J. A. Bookbinder, 131

Wang, Y. M., & Sheeley, N. R., J. 1994, J. Geophys. Res., 99, 6597, doi: 10.1029/93JA02105

Wolfram Research, Inc. 2023, Mathematica Online, Version 13.3. https://www.wolfram.com/mathematica